Discrimination of Malignant and Benign Breast Lesions Using Quantitative Multiparametric MRI: A Preliminary Study

Kurt Li[1], Archana Machireddy[2], Alina Tudorica[3], Brendan Moloney[4], Karen Y. Oh[3], Neda Jafarian[3], Savannah C. Partridge[5], Xin Li[4], and Wei Huang[4]

[1]International School of Beaverton, Aloha, OR; [2]Center for Spoken Language Understanding, Oregon Health & Science University, Portland, OR; [3]Department of Diagnostic Radiology, Oregon Health & Science University, Portland, OR; [4]Advanced Imaging Research Center, Oregon Health & Science University, Portland, OR; and [5]Department of Radiology, University of Washington, Seattle, WA

Corresponding Author:
Wei Huang, PhD
Advanced Imaging Research Center, Oregon Health & Science
University, Portland, OR 97239;
E-mail: huangwe@ohsu.edu

ABSTRACT

We aimed to compare diagnostic performance in discriminating malignant and benign breast lesions between two intravoxel incoherent motion (IVIM) analysis methods for diffusion-weighted magnetic resonance imaging (DW-MRI) data and between DW- and dynamic contrast-enhanced (DCE)-MRI, and to determine if combining DW- and DCE-MRI further improves diagnostic accuracy. DW-MRI with 12 b-values and DCE-MRI were performed on 26 patients with 28 suspicious breast lesions before biopsies. The traditional biexponential fitting and a 3-b-value method were used for independent IVIM analysis of the DW-MRI data. Simulations were performed to evaluate errors in IVIM parameter estimations by the two methods across a range of signal-to-noise ratio (SNR). Pharmacokinetic modeling of DCE-MRI data was performed. Conventional radiological MRI reading yielded 86% sensitivity and 21% specificity in breast cancer diagnosis. At the same sensitivity, specificity of individual DCE- and DW-MRI markers improved to 36%–57% and that of combined DCE- or combined DW-MRI markers to 57%–71%, with DCE-MRI markers showing better diagnostic performance. The combination of DCE- and DW-MRI markers further improved specificity to 86%–93% and the improvements in diagnostic accuracy were statistically significant ($P < .05$) when compared with standard clinical MRI reading and most individual markers. At low breast DW-MRI SNR values (<50), like those typically seen in clinical studies, the 3-b-value approach for IVIM analysis generates markers with smaller errors and with comparable or better diagnostic performances compared with biexponential fitting. This suggests that the 3-b-value method could be an optimal IVIM-MRI method to be combined with DCE-MRI for improved diagnostic accuracy.

INTRODUCTION

High false-positive rate in breast cancer diagnosis using standard-of-care imaging methods, including mammography, ultrasonography, and magnetic resonance imaging (MRI), remains a significant healthcare problem, resulting in unnecessary biopsies of many benign lesions. The American College of Radiology (ACR) MRI Breast Imaging Reporting and Data System (BI-RADS) lexicon (1) is routinely used in standard of care for diagnosis of MRI-detected lesions. This approach mainly relies on interpretations of lesion morphology and qualitative assessment of contrast uptake and washout in the lesion (1). It is well known that breast MRI, as is currently used in clinical practice, has higher sensitivity and comparable, but low, specificity for cancer

detection, when compared with mammography and ultrasonography (2–6). This, in addition to the high cost generally associated with an MRI examination, limits the use of MRI for breast cancer screening to the high-risk population (5–8). Therefore, it is important to improve diagnostic specificity and overall accuracy for MRI to be a valuable and widely used imaging tool for breast cancer diagnosis.

Two quantitative MRI techniques, dynamic contrast-enhanced (DCE) MRI and diffusion-weighted (DW) MRI, have been extensively investigated as a means to improve diagnostic accuracy for breast cancer. The quantitative parameters estimated from pharmacokinetic (PK) modeling of DCE-MRI time-course data, such as K^{trans} (volume transfer rate constant) and

k_{ep} (efflux rate constant), have been shown to be promising imaging markers for improving discrimination of malignant and benign breast lesions (9–11). Likewise, the imaging marker obtained from DW-MRI, apparent diffusion coefficient (ADC), has also been shown useful for improving specificity in breast cancer detection (12, 13). DCE-MRI primarily measures microvascular perfusion and permeability, while DW-MRI can be used to assess cellularity and cell membrane integrity. Because breast lesions are complex systems characterized by spatial and temporal heterogeneity in pathophysiology, a quantitative imaging method that depicts only one aspect of tumor biology is intrinsically limited. Increasing evidence from recent studies (14, 15) shows that by interrogating multifaceted tumor biology, a multiparametric MRI approach provides better diagnostic performance for breast cancer than an individual MRI method. Majority of the reported multiparametric methods combine the information from DCE- and DW-MRI and show improved diagnostic accuracy compared with DCE- or DW-MRI alone (16–22).

In the past decade, one variant of DW-MRI in data acquisition and analysis, intravoxel incoherent motion (IVIM) MRI, which decodes contributions from tissue diffusivity and microcapillary perfusion to DW-MRI signal attenuation (23, 24), has become an emerging technique for breast tumor characterization and has been applied for breast cancer diagnosis (25–32) and therapeutic monitoring (33–35). One attractive feature of the IVIM-MRI method is that tissue diffusion and perfusion can be assessed at once in one imaging sequence without the need for contrast agent injection. The conventional approach for IVIM is to acquire the data with many b-values (diffusion weighting factors) to sensitize the signal to both microcapillary perfusion and tissue diffusion, and fit the data with a biexponential model to extract the following three parameters: true molecular diffusion coefficient (D), perfusion-related pseudodiffusion coefficient (D*), and perfusion fraction (f_p). A segmented fitting approach (36) was recently proposed as an alternative method to improve the precision of IVIM data fitting. However, both fitting methods generally require the use of >10 b-values, which results in long data acquisition time. In a recent study (37), a systemic comparison of IVIM analysis using a range of b-values from 4 to 10 indicated that a reduced number of b-values for IVIM analysis may not compromise the performances of IVIM parameters in characterizing breast tumors. Jalnefjord et al. proposed a 3-b-value approach (38) in IVIM parameter quantification by directly calculating the D and f_p parameters. This approach provides a simple quantitative method that completely avoids nonlinear fitting and the ill-conditioned problem (39) in biexponential fitting, with the drawback of being unable to derive the D* parameter. The latter is well known to be problematic in deriving accurate model parameters from data with low signal-to-noise ratio (SNR), which is often seen in breast DW-MRI performed in routine clinical studies. Furthermore, breast IVIM-MRI studies in the literature (12, 13) have shown that, among the three IVIM parameters, D* is the least robust in characterizing tumor pathology. Therefore, the 3-b-value approach could potentially be an optimal breast IVIM-MRI method, allowing reduced acquisition time and patient discomfort without compromising diagnostic performance.

In this preliminary study, we performed quantitative DW- and DCE-MRI studies in a patient cohort with suspicious breast lesions. The goal was two-fold: comparing the diagnostic performance in discriminating malignant and benign lesions between the two IVIM methods of biexponential fitting and 3-b-value calculation, as well as between DW- and DCE-MRI; and investigating whether combinations of DW-MRI markers (ADC and IVIM parameters) and DCE-MRI PK parameters further improve diagnostic accuracy compared with individual MRI methods or markers.

METHODOLOGY
Patient Cohort
Twenty-six female patients were recruited and consented to participate in a local IRB (Institutional Review Board)-approved research MRI study that included DW- and DCE-MRI. Twenty-eight suspicious lesions in these women (one with 2 lesions in the right and 1 lesion in the left breast) were found by routine mammography and/or ultrasonography screening and diagnosis with ACR BI-RADS scores of 4 or 5, and were referred for biopsies as per standard of care. The MRI studies were performed before the biopsy procedures. Patient demographic and lesion clinicopathologic characteristics are shown in Table 1.

Table 1. Patient Demographic and Lesion Clinicopathologic Characteristics

Characteristic	Number or Mean (range)
Age	50 (22–77 years)
Lesion size in the longest diameter (measured by mammography or ultrasonography)	19 (4–55 mm)
ACR BI-RADS score (mammography or ultrasonography)	
4	27
5	1
ACR BI-RADS score (MRI)	
Positive finding	
4	22
5	1
Negative finding	
3	4
2	1
Biopsy histopathology	
Malignant	14
IDC, grade 1	3
IDC, grade 2	5
IDC, grade 3	2
DCIS, high grade	1
ILC, grade 1	1
ILC, grade 2	1
IMC, grade 2	1
Benign	14

Abbreviations: IDC, invasive ductal carcinoma; DCIS, ductal carcinoma in situ; ILC, invasive lobular carcinoma; IMC, invasive mammary carcinoma

MRI Data Acquisition

All the MRI studies were performed using a 3 T Siemens Prisma system (Siemens Healthcare GmbH, Erlangen, Germany) with the body coil and a 16-channel bilateral phased-array breast coil as the transmitter and receiver, respectively. In each MRI session, scout imaging, axial T2-weighted MRI with fat saturation, and axial T1-weighted MRI without fat saturation were followed by DW-MRI and then DCE-MRI (both with fat saturation). Both DW- and DCE-MRI images were acquired in the axial orientation with bilateral, full breast coverage.

DW-MRI was performed using a single-shot 2D spin-echo EPI sequence with 12 b-values (0, 10, 25, 50, 75, 100, 150, 250, 450, 800, 1000, and 1200 s/mm^2) applied in three orthogonal directions, with the following parameters: echo time (TE) = 68 milliseconds and repetition time (TR) = 6400 milliseconds, in-plane matrix size = 192 × 192, field of view (FOV) = 32–34 cm, slice thickness (no gap) = 5 mm, number of averages = 3, and a parallel imaging acceleration factor of 2 for a total acquisition time of ∼9 minutes.

DCE-MRI was performed using a 3D spoiled gradient echo-based TWIST (Time-resolved angiography WIth Stochastic Trajectories) sequence with water excitation only, which uses the strategy of k-space undersampling during acquisition and data sharing during reconstruction (40). DCE-MRI acquisition parameters included a 10° flip angle (α), TE/TR = 2.9/6.2 milliseconds, parallel imaging acceleration factor of 2, FOV = 32–34 cm, in-plane matrix size = 320 × 320, and slice thickness = 1.4 mm. The total acquisition time for a DCE-MRI scan was ∼10 min for 32–40 frames of image volume containing 96–128 slices each and having a temporal resolution of 14–18 seconds. The variations in the number of frames, number of slices per frame, and temporal resolution were due to differences in breast size. The intravenous injection of a contrast agent, Gd(HP-DO3A) [ProHance (Bracco Diagnostic Inc., Monroe Township, NJ)] at the dose of 0.1 mmol/kg and a rate of 2 mL/s, by a programmable power injector, was timed to commence after the acquisition of two baseline image frames, followed by a 20-mL saline flush.

To quantify the precontrast native T_1 value, T_{10}, for PK analysis of DCE-MRI data, proton density-weighted MRI that was spatially coregistered with DCE-MRI was performed immediately before DCE-MRI. The data acquisition sequence and parameters were the same as those for the DCE-MRI scan except for α = 2° and TR = 50 milliseconds.

IVIM-MRI Simulations

A noiseless biexponential IVIM decay curve was created using breast tumor parameter values for D, D*, and f_p reported in the literature (30). Ten thousand Monte Carlo simulation runs were performed at each SNR, where random Gaussian noise was added to each run. In each simulation, the IVIM parameters were obtained by using standard biexponential fitting (23) [Equation [1], where S and S_0 are signal intensities with and without diffusion weighting, respectively] with 12 b-values (0, 10, 25, 50, 75, 100, 150, 250, 450, 800, 1000, and 1200 s/mm^2) and by using the 3-b-value (0, 200, 800 s/mm^2) method (38) [Equations [2] and [3], where b_1, b_2, b_3 are 0, 200, and 800 s/mm^2, respectively; est: estimate]. Ten SNR levels evenly spaced from 10 to 100 were

simulated. Mean and standard deviation (SD) of the derived parameter values at each SNR level were calculated. The D and f_p values, which were derived from both the 12 b-value biexponential fitting and 3-b-value approach, were then compared with the reference values used to generate the original noiseless curve. The absolute relative error, the absolute difference (between the mean of calculated value and the reference value) over the reference value, was calculated.

$$S = S_0 \left[f_p \exp(-bD^*) + (1 - f_p)\exp(-bD) \right] \qquad [1]$$

$$D_{est} = \frac{1}{b_3 - b_2} \ln \frac{S(b_2)}{S(b_3)} \qquad [2]$$

$$f_{p,est} = 1 - \frac{1}{S(b_1)} \left(\frac{S(b_2)^{b_3}}{S(b_3)^{b_2}} \right)^{\frac{1}{b_3 - b_2}} \qquad [3]$$

We also used mean squared error (MSE) to compare the two analysis approaches. Using the standard approach of bias-variance decomposition (41), the MSE can be calculated as $E^2 + V$, where E (the bias) and V (the variance) can both be calculated from the simulation runs. The method with a smaller MSE value indicates better overall performance in accuracy and precision of parameter estimation.

MRI Data Analysis

Clinical MRI Interpretation. All 28 mammography- and/or sonography-detected suspicious lesions exhibited MRI contrast enhancement and were identified by either of the two radiologists (KYO or NJ; each with >5 years' experience in reading breast MRI) on postcontrast DCE-MRI images. The second baseline image frame and 5 postcontrast image frames were selected from the high temporal resolution TWIST DCE-MRI series to form a new dynamic series with a time interval (or effective temporal resolution) of 70–72 seconds between two consecutive image frames, closely replicating the institutional clinical breast DCE-MRI protocol which uses a conventional full-k-space sampling 3D gradient echo sequence. The newly formed image series were then submitted to a computer-aided diagnosis (CAD) system (DynaCad Breast®, Invivo, Gainesville, FL) for qualitative assessment of contrast kinetics via examination of the curve shape of signal intensity-time course. For each patient, the lesion(s) was evaluated by one radiologist in morphology (from postcontrast DCE-MRI and precontrast T1- and T2-weighted images) and contrast kinetics according to ACR MRI BI-RADS lexicon (1), and assigned an integer BI-RADS score (Table 1). A BI-RADS score of ≥4 was defined as a positive finding, whereas a score of ≤3 was defined as a negative finding. The radiologist was blinded to the pathology results of the biopsy specimens when interpreting the MRI images.

DCE-MRI. The breast lesion regions of interest (ROIs) were manually traced by the radiologists on postcontrast (∼140 seconds after the contrast injection) DCE-MRI image slices that contained the contrast-enhanced lesion. The following procedures for quantitative DCE-MRI data analysis were performed on voxel-by-voxel basis.

Assuming TE $\ll$ T$_2^*$, which was the case for this DCE-MRI study, the signal intensity, S, of a spoiled gradient echo sequence is given by Equation [4]:

$$S = S_0 \sin \alpha \frac{1 - \exp(-TR \cdot R_1)}{1 - \cos \alpha \exp(-TR \cdot R_1)}, \qquad [4]$$

where S_0 is proportional to the proton density of the sample. Used in PK modeling of DCE-MRI data, the voxel T_{10} (= $1/R_{10}$) values were determined with Equation [4] by dividing the signal intensities of the proton density-weighted images by those of the second-frame baseline images from the DCE-MRI series (40, 42). The voxel DCE-MRI signal intensity-time course was then, with the knowledge of R_{10}, converted to R_1 time course, $R_1(t)$, which was fitted to the 2-compartment–3-parameter fast exchange regime (FXR)–allowed shutter-speed PK model (43, 44), expressed in Equation [5]:

$$
\begin{aligned}
R_1(t) = (1/2)\Big[\{2R_{1i} + &\ r_1 K^{trans}/v_e \int_o^t C_p(t') \\
\times \exp\big(-K^{trans}/v_e(t-t')\big)dt' + &\ (R_{10} - R_{1i} + 1/\tau_i)/v_e\} \\
- \{[2/\tau_i + (R_{1i} - R_{10} - 1/\tau_i)/v_e - &\ r_1 K^{trans}/v_e \int_o^t C_p(t') \\
\times \exp\big(-K^{trans}/v_e(t-t')\big)dt']^2 + &\ 4(1-v_e)/\tau_i^2 v_e\}^{1/2}\Big],
\end{aligned}
\qquad [5]
$$

where $C_p(t')$ is the arterial plasma contrast agent concentration time course or arterial input function (AIF); R_{1i} is the intrinsic intracellular longitudinal relaxation rate constant and is assumed to be equal to the tissue R_{10}; r_1 is the contrast agent relaxivity at 3 T, set at 3.8 mM^{-1}s^{-1}; v_e is the volume fraction of extravascular and extracellular space; and τ_i is the mean intracellular water lifetime ($k_{io} = 1/\tau_i$, water efflux rate constant, was quantified and reported in this study). k_{ep} was calculated as $k_{ep} = K^{trans}/v_e$. The FXR shutter-speed model takes into account water exchange kinetics between the intra- and extracellular compartments in the extravascular space (43, 44).

A population-averaged AIF was used for the PK analysis. This AIF was obtained by averaging individually measured AIFs from an axillary artery in a previous prebiopsy breast DCE-MRI study (10) performed with unilateral coverage in the sagittal orientation and higher temporal resolution (<7 seconds), but with the same contrast injection protocol, including dose, injection rate, and injection site (antecubital vein). Voxel values of K^{trans}, v_e, k_{ep}, and k_{io} were estimated from the PK analysis and the corresponding voxel-based parametric maps were generated. The mean lesion PK parameter value was calculated by averaging all the voxel parameter values within the lesion ROIs which were registered from the postcontrast images onto the parametric maps.

DW-MRI. Lesion ROIs were drawn on DW-MRI images in reference to those drawn on postcontrast DCE-MRI images. The voxel-based DW-MRI data were analyzed three times and parametric maps were generated: once with the biexponential IVIM fitting (Equation [1]) with all the b-values up to 1000 s/mm^2 (a total of 11 b-values) to extract D, D*, and f_p; once with the 3-b-value approach (0, 200, 800 s/mm^2) (38) (Equations [2] and [3]) to extract D_{est} and $f_{p,est}$; and once with monoexponential fitting with 2 b-values (0 and 800 s/mm^2) to extract ADC. The lesion

mean parameter value was calculated by averaging all the voxel values within the lesion ROIs which were registered from the DW-MRI images onto the parametric maps.

Statistical Analysis

Descriptive statistical analysis was performed for individual DW- and DCE-MRI markers. To determine if there was a significant difference in each marker between the malignant and benign lesions, a two-sample unpaired t test was performed to calculate the t-statistic and P values. Paired sample t test was performed on the DW-MRI markers from the entire cohort to determine if different approaches in DW-MRI data analysis resulted in significant differences between the corresponding markers: D vs D_{est} and f_p vs $f_{p,est}$, as well as D vs ADC and D_{est} vs ADC.

A linear support vector machine (SVM) (45) was used to generate a predictive model for classification of malignant and benign lesions. The predictive performance was assessed as ROC (receiver operating characteristic) AUC (area under the curve) for each individual imaging marker separately and for a combination of imaging markers. The combined markers were constructed by concatenating individual markers to form feature vectors with multiple dimensions as follows: IVIM1, combining D, D*, and f_p; IVIM2, combining D_{est} and $f_{p,est}$; DCE, combining K^{trans}, k_{ep}, v_e, and k_{io}; DCE + ADC, four DCE-MRI markers and ADC; DCE + IVIM1, four DCE-MRI and three IVIM (D, D*, and f_p) markers; and DCE + IVIM2, four DCE-MRI, and two IVIM (D_{est} and $f_{p,est}$) markers. Pairwise comparisons of ROC AUC values for all the markers were performed by calculating the critical ratio according to the Hanley and McNeil formula (46). In addition to the classification results, the SVM generated a score indicating the likelihood of an individual or combined marker value representing a malignant or benign lesion. These scores were sorted and cutoff values were selected to achieve the same sensitivity in discriminating malignant and benign lesion as that from the clinical MRI reading, and the specificity values were then calculated accordingly.

Pearson correlation analysis was performed for the diffusion and perfusion imaging markers, within and between the DW- and DCE-MRI methods. Pearson correlation coefficients and P values were calculated.

The statistical significance was set at $P < .05$ for all the aforementioned statistical analyses.

RESULTS

Histopathological analysis of the biopsy specimens revealed that 14 lesions were malignant and the other 14 lesions were benign (Table 1).

DW-MRI SNR was estimated for each voxel within the lesions ROIs using the multiframe method (47), in which the voxel SNR was calculated as the mean of signal intensities from images obtained with three orthogonal diffusion weightings at b = 10 s/mm^2 over the standard deviation of signal intensities from the same images. The selection of the images with the lowest diffusion weighting used in this study was intended to estimate the highest possible SNR in the DW-MRI images (except for those with b = 0 s/mm^2). Combining all voxel SNR

Figure 1. The absolute relative errors (A and B) and mean parameter values (C and D) from the simulations are plotted against signal-to-noise ratios (SNRs) for the intravoxel incoherent motion (IVIM) parameter pairs of D and D_{est} (A and C) and f_p and $f_{p,est}$ (B and D). The D and f_p parameters from the 12-b-value bi-exponential fitting are shown in black circles, while the D_{est} and $f_{p,est}$ parameters from the 3-b-value approach are shown in light-gray triangles. Each data point represents the average of 10 000 iterations of the simulations. The error bar in C and D represents standard deviation from the simulations.
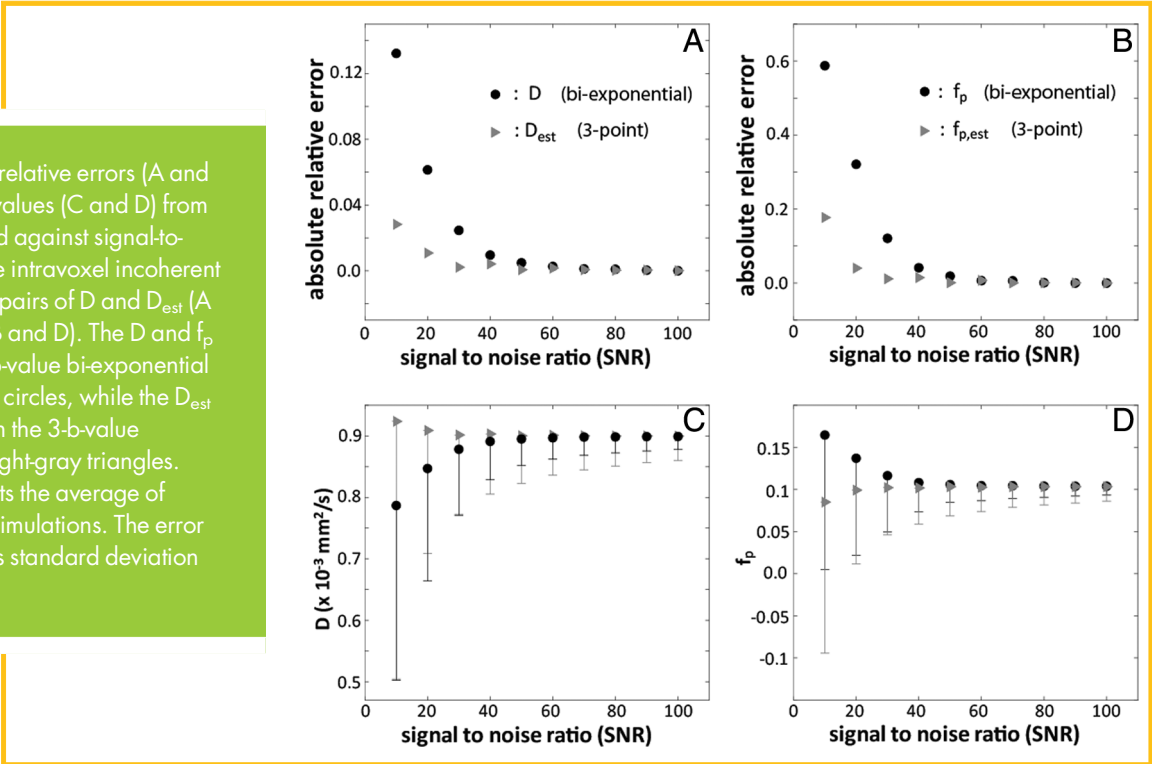
values across all available lesion ROIs and all the patients resulted in SNR = 36.9 ± 18.4 (mean ± SD) for the breast DW-MRI data sets.

IVIM-MRI Simulations

Panels A and B in Figure 1 compare the absolute relative errors at different SNRs in the IVIM parameters derived in simulations of the two analysis approaches, between D and D_{est} (A), f_p and $f_{p,est}$ (B), respectively. The 3-b-value estimated values are shown in light gray, while the 12 b-value biexponential fitting results are in black, with each data point representing the average of 10 000 iterations of the simulations. Absolute relative errors for both sets of parameters decrease with increasing SNR. When SNR < 50, the 12-b-value biexponential fit generates larger parameter errors than the 3-b-value fit. The errors from the two fitting approaches converge and reach a plateau near zero when SNR ≥ 60. With the same representations, panels C and D in Figure 1 show the calculated mean D and D_{est} and f_p and $f_{p,est}$ values, respectively, at different SNRs, with associated error bars representing SD from the simulations. It is clear that simulated parameter values from the 3-b-value and 12-b-value methods converge to the reference value from different directions. For the 12-b-value biexponential fitting, the D and f_p parameters converge to the reference values from under- and overestimations, respectively, with increasing SNR. The opposite is observed for the 3-b-value method. Although the 3-b-value calculations generate parameter values closer to the references values than the 12-b-values biexponential fitting at low SNRs, the SD values from the simulations are actually larger.

Figure 2 shows plots of MSE vs SNR for D and D_{est} (Figure 2A) and f_p and $f_{p,est}$ (Figure 2B), respectively. The lines through

the data points are meant to guide the eyes only. When comparing 12-b-value biexponential fitting with the 3-b-value approach at the same SNR, the overall performance of parameter accuracy and precision, as measured by MSE, of the former is generally better. However, when correcting for total image acquisition time, that is, making the acquisition time of 3-b-value DW-MRI equal to that of 12-b-value DW-MRI by increasing or decreasing the signal averaging of the former or latter, respectively, the effective SNR for the 3-b-value approach could be two times higher than that of the 12-b-value method. Therefore, the results in Figure 2 suggest that the 3-b-value approach could be better than the 12-b-value method in estimated parameter accuracy and precision at low SNR under the same acquisition time. For example, comparison of the 3-b-value method at SNR = 40 with the 12-b-value method at SNR = 20 in Figure 2 shows that MSE values of both D_{est} and $f_{p,est}$ are smaller than those of D and f_p, respectively.

DW-MRI

The mean ± SD values of ADC, D, D_{est}, f_p, and $f_{p,est}$ for the entire 28-lesion cohort are shown in Table 2, as well as the P values for pairwise comparisons among ADC, D, and D_{est} and between f_p and $f_{p,est}$. D* is not listed for comparison, as the 3-b-value method does not generate this parameter. Both ADC and D_{est} were significantly (P < .05) larger than D, while there was no significant difference between ADC and D_{est}. $f_{p,est}$ was significantly (P < .05) smaller than f_p.

Diagnostic Performance

The clinical interpretation of the MRI data generated 23 positive and 5 negative findings (Table 1), which, following correlations with histopathology results (Table 1), gave 12 true positives, 2
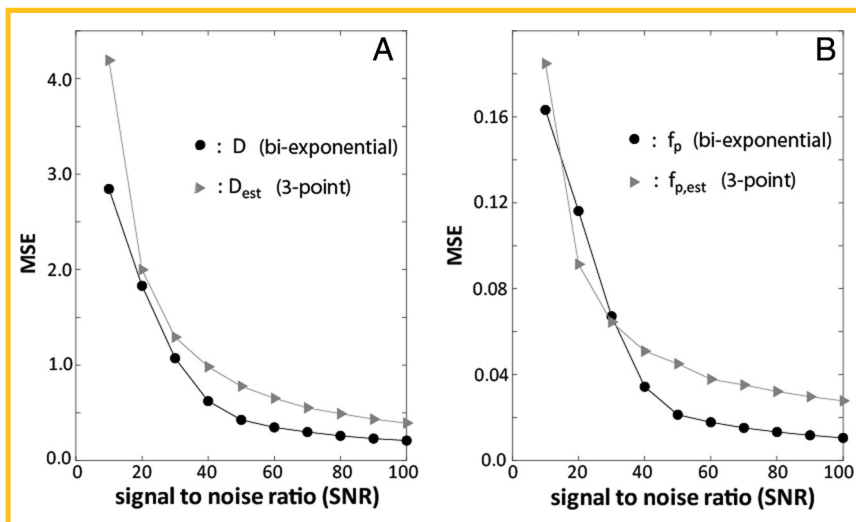
Figure 2. The mean squared error (MSE) values are plotted against SNRs for the parameter pairs of D and D_{est} (A) and f_p and $f_{p,est}$ (B). The symbol representations are the same as those in Figure 1. The lines through the data points are meant to guide the eyes only.

false negatives, 3 true negatives, and 11 false positives. Therefore, the sensitivity and specificity for discriminating malignant and benign lesions from clinical MRI reading were 86% and 21%, respectively.

Table 3 lists the mean ± SD values of all individual imaging markers for the malignant and benign lesion groups, obtained from PK modeling of DCE-MRI data and analysis of DW-MRI data with different approaches (monoexponential ADC fitting, biexponential IVIM fitting, and the 3-b-value IVIM analysis). The malignant lesions exhibited significantly ($P < .05$) higher K^{trans} and k_{ep} and lower ADC and D_{est} values compared with the benign lesions. No statistically significant differences between the two lesion groups were found in the other markers. Figure 3 shows postcontrast DCE-MRI image slices (the middle two panels) and the voxel-based color parametric maps of ADC, D_{est}, D, $f_{p,est}$, f_p, D^*, K^{trans}, k_{ep}, v_e, and k_{io} from a malignant (top two rows) and a benign (bottom two rows) lesion. The DCE-MRI parametric maps were from the same postcontrast DCE-MRI image slice which was through the central portion of the lesion, while the DW-MRI parametric maps were from a slightly different image slice location owing to the difference in slice thickness between the DCE- and DW-MRI acquisitions. The color scale for each parameter was kept the same for comparing the two lesions. It can be visually observed that, compared with the benign lesion, the malignant lesion exhibited higher K^{trans} and k_{ep} but lower ADC, D_{est}, and D values.

Table 4 shows the ROC AUC, sensitivity, and specificity values for discriminating malignant and benign lesions for all the individual and combined imaging markers. Because the sensitivity of clinical MRI reading was 86%, the specificities for the quantitative imaging markers (individual or combined) were calculated with sensitivity kept at 86% for fair comparisons. Among the individual markers, K^{trans}, k_{ep}, D_{est}, and ADC showed high diagnostic accuracies with 0.70–0.80 ROC AUC and 36%–57% specificity, while v_e, D^*, f_p, and $f_{p,est}$ showed low diagnostic accuracies with 0.50–0.57 ROC AUC and 14%–28% specificity, similar to clinical MRI reading with 0.56 ROC AUC and 21% specificity. Within DCE-MRI or each of the two IVIM-MRI analysis methods, the combination of the imaging markers, DCE, IVIM1, and IVIM2, improved diagnostic performance with 0.76–0.88 ROC AUC and 57%–71% specificity. In general, DCE-MRI outperformed DW-MRI, individual or combined markers, in discriminating malignant and benign lesions. The diagnostic accuracy was further improved when DCE-MRI markers were combined with DW-MRI markers, DCE + ADC, DCE + IVIM1, and DCE + IVIM2, with 0.92–0.93 ROC AUC and 86%–93% specificity.

Table 5 shows the P values from pairwise comparisons of ROC AUC values among all the individual and combined imaging markers. Combined DCE-MRI markers or combined DCE- and DW-MRI markers (DCE or DCE + ADC, DCE + IVIM1, and DCE + IVIM2) showed significantly ($P < .05$) better diagnostic performance in discriminating malignant and benign lesions, as measured by ROC AUC, compared with standard clinical MRI reading. In general, the combined DCE- and DW-MRI markers showed significantly ($P < .05$) higher ROC AUC compared with

Table 2. DW-MRI Parameters (Mean ± SD) and Pairwise Comparisons (P Value)

	ADC	D	D_{est}	f_p	$f_{p,Est}$
Mean ± SD	1.08 ± 0.60	0.65 ± 0.54	1.06 ± 0.57	0.29 ± 0.22	0.10 ± 0.07
P	6.3×10^{-7} *	7.0×10^{-7} **	0.48 #	9.9×10^{-5} ***	—

Units for ADC, D, and Dest: $\times 10^{-3}$ mm^2/s.
Paired t test: *ADC vs D; **D vs Dest; ***fp vs fp,est; #ADC vs Dest.

Table 3. DW-MRI and DCE-MRI Parameter Values for Malignant and Benign Lesions (Mean ± SD)

Lesion	$D (\times 10^{-3}$ $mm^2/s)$	$D^* (\times 10^{-2}$ $mm^2/s)$	f_p	$D_{est} (\times 10^{-3}$ $mm^2/s)$	$f_{p,est}$	$ADC (\times 10^{-3}$ $mm^2/s)$	K^{trans} (min^{-1})	k_{ep} (min^{-1})	v_e	$k_{io} (s^{-1})$
Malignant	0.51 ± 0.44	3.38 ± 2.75	0.24 ± 0.23	0.80 ± 0.49^a	0.11 ± 0.08	0.83 ± 0.54^a	0.25 ± 0.14^a	4.72 ± 4.36^a	0.30 ± 0.32	2.57 ± 0.77
Benign	0.80 ± 0.62	3.07 ± 2.53	0.35 ± 0.20	1.32 ± 0.54	0.10 ± 0.06	1.33 ± 0.57	0.12 ± 0.10	2.05 ± 2.91	0.39 ± 0.33	2.27 ± 0.87

^{a} $P < 0.05$, statistically significant difference, unpaired t test comparing the malignant and benign lesions.

any individual markers except for K^{trans} and D_{est}, which had high ROC AUC values themselves (Table 4). No statistically significant difference was found in pairwise ROC AUC comparison among the individual markers, IVIM1, IVIM2, and clinical MRI reading; or among the combined markers—IVIM1, IVIM2, DCE, DCE + ADC, DCE + IVIM1, and DCE + IVIM2.

Imaging Marker Correlation

Pearson correlation coefficient and *P* values for pairwise correlations among all the diffusion markers of ADC, D, and D_{est}, and perfusion markers of K^{trans}, k_{ep}, f_p, $f_{p,est}$, and D^* are listed in Table 6. Within DW-MRI, ADC, D, and D_{est} showed strong significant ($P \leq 1.0 \times 10^{-7}$) positive correlations between each other; while there were also significant ($P < .05$) positive correlations in ADC vs D^* and ADC vs f_p, as well as D vs D^*. The DCE-MRI perfusion markers K^{trans} and k_{ep} also showed significant ($P < .05$) positive correlation. However, there were no significant correlations among the perfusion markers from IVIM-MRI (f_p, $f_{p,est}$, and D^*) and across IVIM- and DCE-MRI (f_p, $f_{p,est}$, or D^* vs K^{trans} or k_{ep}). Unlike D and D_{est}, which were significantly correlated, there was no significant correlation between f_p and $f_{p,est}$ derived with the biexponential and 3-b-value IVIM analysis methods, respectively.

DISCUSSION

Although not statistically significantly better in diagnostic performances in comparison with clinical MRI reading, D, D_{est}, and ADC from DW-MRI and K^{trans} and k_{ep} from DCE-MRI are promising individual diagnostic markers for breast cancer, showing substantially greater ROC AUC and specificity (under the same sensitivity of 86%) values in discriminating malignant and benign lesions. The worst-performing markers, such as D^*, f_p, and v_e, had diagnostic accuracies similar to clinical MRI reading. Consistent with previous IVIM-MRI studies for breast cancer diagnosis (12, 13), the D parameter is the most robust among the three IVIM markers for discriminating malignant and benign breast lesions. This preliminary study shows that D_{est}, derived with the 3-b-value method, has better diagnostic capability (although not statistically significant) than D, derived with the traditional biexponential IVIM fitting. Along with ADC, K^{trans}, and k_{ep}, D_{est} was another individual marker that exhibited statistically significant difference in value between malignant and benign lesions. This suggests that a 3-b-value approach for IVIM-MRI may be optimal for the purpose of breast cancer diagnosis, which has the added benefit of reduced data acquisition time and patient discomfort.

Combining individual imaging markers within each MRI method clearly improved diagnostic performance compared to any individual markers. Although there were no statistically significant differences in ROC AUC among the combined markers of IVIM1, IVIM2, and DCE, the superiority of DCE over standard clinical MRI reading for discriminating malignant and benign lesions was statistically significant (Table 5). Whether comparing individual or combined markers, quantitative DCE-MRI PK parameters outperformed quantitative DW-MRI markers (ADC or IVIM parameters) in accuracy for breast cancer diagnosis. Therefore, in the foreseeable future, it is unlikely that noncontrast DW-MRI (with the capacity for IVIM analysis) will replace DCE-MRI for diagnosis of breast cancer without fundamental improvements in DW-MRI data acquisition and analysis.

In agreement with previous studies (16–22, 27, 31), this study shows that the multiparametric approach of combining DCE-MRI and DW-MRI (ADC or IVIM parameters) markers further improves diagnostic accuracy in discriminating malignant and benign lesions when compared with each individual MRI method. The diagnostic performances of DCE + IVIM1, DCE + IVIM2, and DCE + ADC were statistically significantly better than clinical MRI reading and any individual imaging markers except for D_{est} and K^{trans}, which were the two best individual diagnostic markers. This study differs from the previous multiparametric studies (16–22, 27, 31), in that quantitative PK parameters were used as DCE-MRI markers here while qualitative or semiquantitative kinetic parameters were used in those studies. Even though the D^* parameter was missing from the 3-b-value IVIM analysis method, the diagnostic performance of the combined markers DCE + IVIM2 was essentially the same as that of DCE + IVIM1, suggesting that, compared with the biexponential fitting approach with >10 b-values, the 3-b-value IVIM method is adequate when combined with DCE-MRI for breast cancer diagnosis, at least at SNR < 50, which was the case in this study.

To the best of our knowledge, there are two studies (28, 29) that used and compared quantitative IVIM markers and DCE-MRI PK parameters for discriminating malignant and benign breast lesions. Unlike this preliminary study, none of the two studies combined IVIM and PK parameters to improve diagnostic performances. Liu et al. (28) found moderate correlation of f_p with v_p [plasma volume fraction, derived with extended Tofts model (48)], but not with K^{trans} or k_{ep}. Jiang et al. (29) did not find any significant correlations between IVIM- and DCE-MRI parameters. Because insufficient DCE-MRI temporal resolution causes high variability in v_p estimation (49), v_p was not included as a model variable in PK analysis of our DCE-MRI data. In
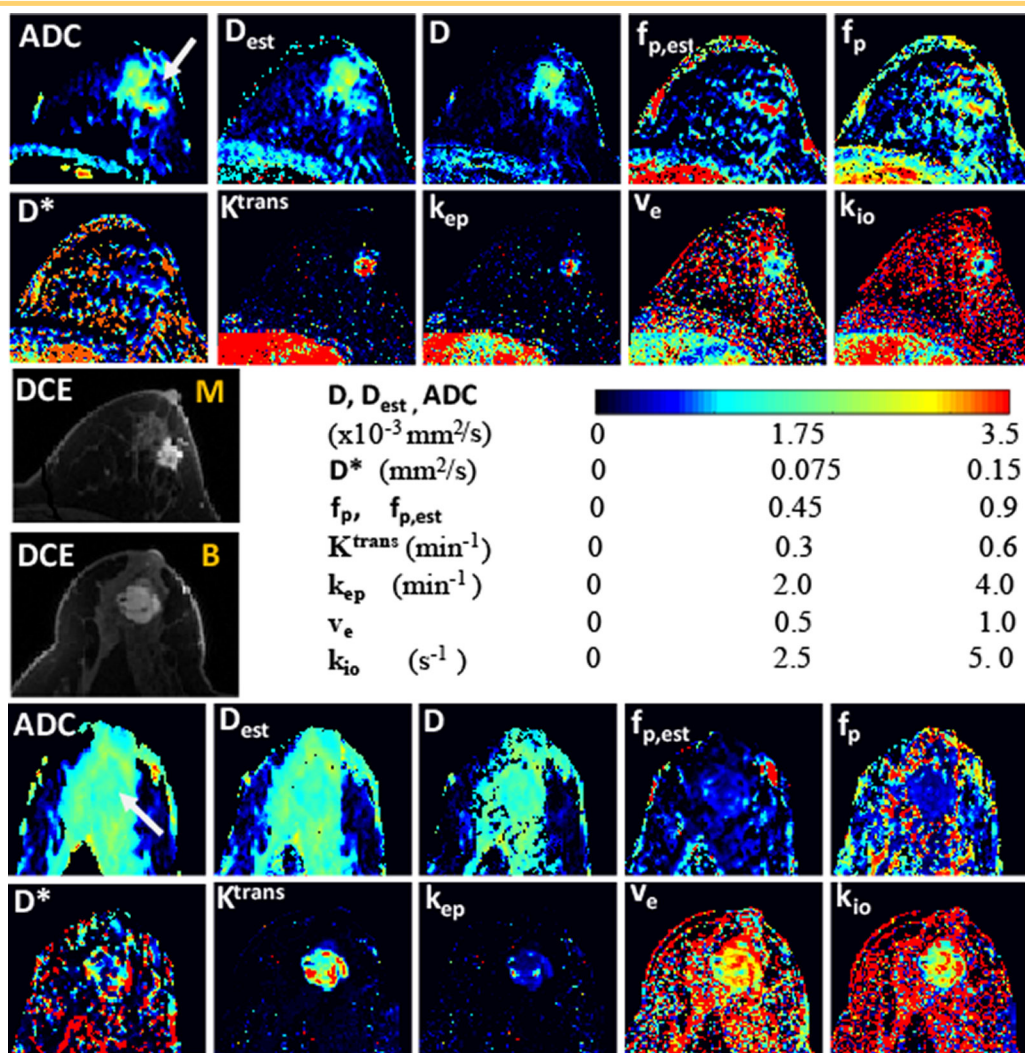
Figure 3. Postcontrast DCE-MRI images exhibiting contrast-enhanced breast lesions are shown in the middle two panels for a malignant (M) (grade 2 invasive ductal carcinoma) and a benign (B) (fibroadenoma) lesion. The voxel-based color parametric maps of ADC, D_{est}, D, $f_{p,est}$, f_p, D^*, K^{trans}, k_{ep}, v_e, and k_{io} from a single image slice are shown for the malignant (top 2 rows) and benign (bottom 2 rows) lesions. The DCE-MRI parametric maps (K^{trans}, k_{ep}, v_e, and k_{io}) were from the same postcontrast image slice which was through the central portion of the lesion, while the DW-MRI parametric maps were from a slightly different image slice location owing to the difference in slice thickness between the DCE- and DW-MRI acquisitions. The arrows in the two ADC maps point to the two lesions, respectively. The color scale for each parameter is kept the same for both lesions.

addition, we used the shutter-speed model-based home-built software and experimentally measured AIF from an artery near the breast for PK data analysis, whereas those two studies used Tofts model-based manufacturer software and a generic population AIF derived from arteries that are not anatomically adjacent to the breast. Despite these differences in PK analysis, the results of our study are consistent with the results of those two studies, in that significant correlations were not observed between the IVIM perfusion parameter, f_p (and $f_{p,est}$ in our study), and the DCE-MRI parameters K^{trans} and k_{ep}. This is probably because f_p represents volume fraction of microcapillaries, while the parameters K^{trans} and k_{ep} are dominated by vessel permeability (44, 48).

The latter may also explain why no correlations were observed between K^{trans} or k_{ep} and D^*, which is related to the microcapillary flow. The lack of associations in perfusion parameters between IVIM- and DCE-MRI supports the multiparametric approach of using IVIM- and DCE-MRI as two independent and yet complementary quantitative MRI methods for improved accuracy in breast cancer diagnosis.

It is well known that fitting of the biexponential decay rate constants (D^* and D in IVIM analysis) is an ill-conditioned problem (39) at low SNR. For IVIM biexponential fitting, the reliabilities of the estimated D^* and D parameters strongly depend on the SNR of the DW-MRI data, as shown by the simulation results.

Table 4. Discrimination of Malignant and Benign Breast Lesions

MRI Methods	ROC AUC	Sensitivity (%)	Specificity (%)
Clinical MRI Reading	0.56	86	21
DW-MRI			
D	0.66	86	36
D*	0.52	86	21
f_p	0.50	86	14
D_{est}	0.76	86	43
$f_{p,est}$	0.56	86	28
ADC	0.71	86	36
DCE-MRI			
K^{trans}	0.80	86	57
k_{ep}	0.70	86	43
v_e	0.57	86	14
k_{io}	0.64	86	28
IVIM1	0.78	86	64
IVIM2	0.76	86	57
DCE	0.88	86	71
DCE + IVIM1	0.92	86	93
DCE + IVIM2	0.93	86	86
DCE + ADC	0.92	86	86

Abbreviations: ROC, receiver operating characteristic; AUC, area under the curve; IVIM1: multivariable combination of D, D*, and f_p; IVIM2: multivariable combination of D_{est} and $f_{p,est}$; DCE: multivariable combination of K^{trans}, k_{ep}, v_e, and k_{io}; DCE + IVIM1: multivariable combination of K^{trans}, k_{ep}, v_e, k_{io}, D, D*, and f_p; DCE + IVIM2: multivariable combination of K^{trans}, k_{ep}, v_e, k_{io}, D_{est}, and $f_{p,est}$; DCE + ADC: multivariable combination of K^{trans}, k_{ep}, v_e, k_{io}, and ADC.

At SNR < 50, which was the case for our DW-MRI data, the accuracies of D and f_p from the biexponential fitting are poorer than those of D_{est} and $f_{p,est}$ from the 3-b-value method (Figure 1). This may explain why D_{est} had a better diagnostic performance than D in discriminating malignant and benign lesions. It is not surprising to see the significant differences in D vs D_{est} and f_p vs $f_{p,est}$ comparisons in the human breast DW-MRI data (Table 2), as the simulations show that each set of the parameters converges to the reference value from the opposite directions with increasing SNR (Figure 1, C and D). f_p is substantially overestimated at low SNR (Figure 1D), which could be the reason why we observed unrealistic f_p values in the human study (Tables 2 and 3). In the 3-b-value approach, the second b-value (200 s/mm^2) is chosen based on the assumption that the pseudoperfusion component is completely decayed at this b-value, and the third b-value (800 s/mm^2) is chosen to avoid appreciable kurtosis effect (50) in the IVIM analysis. Thus, the D_{est} parameter is essentially calculated (Equation [2]) from the linear region in the semilog plot of DW-MRI signal vs b-value curve. This happens to be similar to how ADC is defined and calculated, though the b-values of 0 and 800 s/mm^2 were used in ADC calculation in this study. This similarity in D_{est} and ADC quantification and

the overestimation of D_{est} by the 3-b-value method at low SNR (Figure 1C) explains why we obtained nearly identical breast lesion D_{est} and ADC values. Furthermore, the simulations show that, when both parameter accuracy and precision as measured by $E^2 + V$ (MSE) are taken into consideration (Figure 2), the 3-b-value approach still has the advantage over biexponential fitting with >10 b-values under the conditions of low SNR and equal acquisition time. It is important to note that, in comparing the two analysis approaches, the majority of the b-values used for biexponential fitting were between 0 and 200 s/mm^2 in this study, while most b-values were in the range of 200–800 s/mm^2 in the study by Jalnefjord et al. (38). In addition, the three b-values used in this study for the 3-b-value method were optimized from a DW-MRI study of the liver (38), which likely has different IVIM parameter values compared with malignant and benign breast lesions. Thus, further investigations are needed to determine the optimal b-value distribution for the 3-b-value method that is tailored to the ranges of breast lesion IVIM parameter values.

One clear limitation of this study is the small cohort size. Therefore, the findings are preliminary and need to be validated in a much larger population. The lack of statistically significant difference in diagnostic performance between individual imaging markers, even between the best and worst diagnostic markers, was probably due to the small sample size. The ROC AUC values were essentially the same among the three multiparametric approaches of DCE + IVIM1, DCE + IVIM2, and DCE + ADC for this small cohort. Because the DW-MRI data acquisition time is similar for ADC quantification and for 3-b-value IVIM analysis, it will be interesting to investigate in a larger population whether the DCE + IVIM2 (the 3-b-value method) combination performs better in discriminating malignant and benign breast lesions than the DCE + ADC combination. If not, then ADC quantification from DW-MRI is adequate when combined with DCE-MRI for breast cancer diagnosis. Another limitation of this study is in lesion mean parameter value calculation based on lesion ROIs drawn manually. The DCE-MRI-based and DW-MRI-based ROIs were drawn separately. The contrast between the lesion and surrounding normal tissue was much more prominent on postcontrast DCE-MRI images than DW-MRI images. Even with visual reference to the postcontrast DCE-MRI images, the ROI drawing on DW-MRI images was expected to be less precise and more prone to random errors. As a result, there might have been larger random errors in quantifications of lesion DW-MRI parameters (ADC and IVIM parameters), which contributed to their lower diagnostic performances compared with DCE-MRI markers such as K^{trans}. The differences in in-plane spatial resolution and slice thickness between DW- and DCE-MRI are other confounding factors, in addition to ROI drawing, that affected accuracies in DW- and DCE-MRI parameter quantifications and, consequently, diagnostic performances differently. Lastly, as this study focused on comparing the 3-b-value IVIM method with the traditional biexponential fitting, other IVIM analysis methods such as segmented fitting (36) with >10 b-values were not tested and compared for discriminating malignant and benign lesions.

Table 5. Comparing Diagnostic Performances (*P* Values)

	Clinical reading	D	D*	f_p	D_{est}	$f_{p,est}$	ADC	K^{trans}	v_e	k_{io}	k_{ep}	IVIM1	IVIM2	DCE	DCE + IVIM1	DCE + IVIM2	DCE + ADC
Clinical reading		0.43	0.92	0.34	0.14	0.90	0.23	0.084	0.82	0.48	0.28	0.098	0.11	**0.014***	**0.0004***	**0.0008***	**0.0014***
D			0.37	0.89	0.30	0.36	0.71	0.35	0.58	0.92	0.78	0.24	0.30	0.11	**0.014***	**0.011***	**0.026***
D*				0.29	0.12	0.97	0.20	0.069	0.74	0.42	0.24	0.080	0.12	**0.012***	**0.0011***	**0.0002***	**0.0002***
f_p					0.55	0.28	0.80	0.40	0.48	0.81	0.89	0.28	0.48	0.14	**0.0098***	**0.028***	**0.025***
D_{est}						0.11	0.64	0.77	0.22	0.44	0.67	0.82	0.96	0.36	0.14	0.11	0.17
$f_{p,est}$							0.19	0.063	0.72	0.40	0.22	0.073	0.10	**0.010***	**0.0001***	**0.0010***	**0.0010***
ADC								0.50	0.34	0.63	0.91	0.37	0.56	0.20	**0.049***	**0.045***	0.084
K^{trans}									0.13	0.17	0.42	0.90	0.80	0.48	0.26	0.21	0.24
v_e										0.64	0.40	0.16	0.21	**0.013***	**0.0040***	**0.0008***	**0.0006***
k_{io}											0.70	0.32	0.39	0.073	**0.017***	**0.010***	**0.013***
k_{ep}												0.54	0.63	0.076	**0.045***	**0.011***	**0.010***
IVIM1													0.80	0.46	0.14	0.17	0.23
IVIM2														0.39	0.12	0.085	0.15
DCE															0.68	0.61	0.61
DCE + IVIM1																0.89	1.00
DCE + IVIM2																	0.83
DCE + ADC																	

*$P < 0.05$ (in bold), statistically significant difference in ROC AUC.

CONCLUSION

Both DCE- and DW-MRI provide quantitative imaging markers that are more accurate in discriminating malignant and benign breast lesions than standard clinical MRI reading. In general, individual or combined DCE-MRI markers exhibit better diagnostic performances than individual or combined DW-MRI markers (ADC or IVIM parameters). The combinations of DCE- and DW-MRI markers allow further improvement in breast cancer diagnostic accuracy. In the low SNR range (SNR < 50) typically seen in clinical breast DW-MRI studies, the 3-b-value approach for IVIM analysis generates imaging markers with smaller errors and with comparable or better diagnostic performances when

Table 6. Correlations among the DW- and DCE-MRI Parameters

	ADC	D	D_{est}	D*	f_p	$f_{p,est}$	K^{trans}	k_{ep}
ADC	—	0.82 (1.1×10^{-7})*	0.97 (2.8×10^{-18})*	0.38 (0.046)*	0.51 (0.0058)*	0.053 (0.79)	0.037 (0.85)	−0.28 (0.087)
D	—	—	0.82 (1.0×10^{-7})*	0.63 (0.00031)*	−0.011 (0.95)	−0.14 (0.46)	−0.039 (0.84)	−0.14 (0.48)
D_{est}	—	—	—	0.37 (0.051)	0.36 (0.065)	0.026 (0.90)	−0.035 (0.86)	−0.35 (0.066)
D*	—	—	—	—	−0.21 (0.28)	0.069 (0.73)	−0.10 (0.60)	−0.21 (0.29)
f_p	—	—	—	—	—	0.13 (0.50)	0.083 (0.67)	−0.22 (0.23)
$f_{p,est}$	—	—	—	—	—	—	0.044 (0.82)	0.066 (0.74)
K^{trans}	—	—	—	—	—	—	—	0.42 (0.047)*
k_{ep}	—	—	—	—	—	—	—	—

Pearson correlation coefficient (*P* value).
* $P < .05$, statistically significant correlation.

compared with the traditional biexponential fitting approach. Therefore, the 3-b-value method could be an optimal IVIM-MRI method to be combined with DCE-MRI for improved breast cancer diagnostic accuracy in clinical settings.

REFERENCES

1. American College of Radiology. Breast Imaging Reporting and Data System (BI-RADS): Breast Imaging Atlas, Reston, VA: American College of Radiology (2003).
2. Peters N, Borel Rinkes IHM, Zuithoff NPA, Mali W, Moons KGM, Peeters P. Meta-analysis of MR imaging in the diagnosis of breast lesions. Radiology. 2008;246:116–124.
3. Morrow M, Waters J, Morris E. MRI for breast cancer screening, diagnosis, and treatment. Lancet. 2011;378:1804–1811.
4. DeMartini W, Lehman C, Partridge S. Breast MRI for cancer detection and characterization: a review of evidence-based clinical applications. Acad Radiol. 2008;15:408–416.
5. Menezes GLG, Knuttel FM, Stehouwer BL, Pijnappel RM, van der Bosch M. Magnetic resonance imaging in breast cancer: a literature review and future perspectives. WJCO. 2014;5:61–70.
6. Raikhlin A, Curpen B, Warner E, Betel C, Wright B, Jong R. Breast MRI as an adjunct to mammography for breast cancer screening in high-risk patients: retrospective review. AJR. 2015;204:889–897.
7. Kuhl CK, Schrading S, Leutner CC, Morakkabati-Spitz N, Wardelmann E, Fimmers R, Kuhn W, Schild HH. Mammography, breast ultrasound, and magnetic resonance imaging for surveillance of women at high familial risk for breast cancer. J Clin Oncol. 2005;23:8469–8476.
8. Berg WA, Zhang Z, Lehrer D, Jong RA, Pisano ED, BR, Bohm VM, Mahoney MC, Evans IIW, Larsen LH, Morton MJ, Mendelson EB, Farria DM, Cormack JB, Marques HS, Adams A, Yeh NM, Gabrielli G. Detection of breast cancer with addition of annual screening ultrasound or a single screening MRI to mammography in women with elevated breast cancer risk. JAMA. 2012;307:1394–1404.
9. Sorace AG, Partridge SC, Li X, Virostko J, Barnes SL, Hippe DS, Huang W, Yankeelov TE. Distinguishing benign and malignant breast tumors: preliminary comparison of kinetic modeling approaches using multi-institutional dynamic contrast-enhanced MRI data from the international Breast MR Consortium 6883 trial. J Med Imag. 2018;5:011019.
10. Huang W, Tudorica LA, Li X, Thakur SB, Chen Y, Morris EA, Tagge IJ, Korenblit ME, Rooney WD, Koutcher JA, Springer CS. Discrimination of benign and malignant breast lesions by using shutter-speed dynamic contrast-enhanced MR imaging. Radiology. 2011;261:394–403.
11. Schabel MC, Morrell GR, Oh KY, Walczak CA, Barlow RB, Neumayer LA. Pharmacokinetic mapping for lesion classification in dynamic breast MRI. J Magn Reson Imaging. 2010;31:1371–1378.
12. Partridge SC, Nissan N, Rahbar H, Kitsch AE, Sigmund EE. Diffusion-weighted breast MRI: clinical applications and emerging techniques. J Magn Reson Imaging. 2017;45:337–355.
13. Iima M, Honda M, Sigmund EE, Kishimoto AO, Kataoka M, Togashi K. Diffusion MRI of the breast: current status and future directions. J Magn Reson Imaging. 2019. [Epub ahead of print]
14. Pinker K, Helbich TH, Morris EA. The potential of multiparametric MRI of the breast. Br J Radiol. 2017;90:20160715.
15. Marino MA, Helbich T, Baltzer P, Pinker-Domenig K. Multiparametric MRI of the breast: a review. J Magn Reson Imaging. 2018;47:301–315.
16. Zhang M, Horvat JV, Bernard-Davila B, Marino MA, Leithner D, Ochoa-Albiztegui RE, Helbich TH, Morris EA, Thakur S, Pinker K. Multiparametric MRI model with dynamic contrast-enhanced and diffusion-weighted imaging enables breast cancer diagnosis with high accuracy. J Magn Reson Imaging. 2019;49:864–874.
17. Pinker K, Bickel H, Helbich TH, Gruber S, Dubsky P, Pluschnig U, Rudas M, Bago-Horvath Z, Weber M, Trattnig S, Bogner W. Combined contrast-enhanced magnetic resonance and diffusion-weighted imaging reading adapted to the "Breast Imaging Reporting and Data System" for multiparametric 3-T imaging of breast lesions. Eur Radiol. 2013;23:1791–1802.
18. Baltzer A, Dietzel M, Kaiser CG, Baltzer PA. Combined reading of contrast enhanced and diffusion weighted magnetic resonance imaging by using a simple sum score. Eur Radiol. 2016;26:884–891.
19. Partridge SC, Rahbar H, Murthy R, Chai X, Kurland BF, DeMartini WB, Lehman CD. Improved diagnostic accuracy of breast MRI through combined apparent diffusion coefficients and dynamic contrast-enhanced kinetics. Magn Reson Med. 2011;65:1759–1767.
20. Kul S, Cansu A, Alhan E, Dinc H, Gunes G, Reis A. Contribution of diffusion-weighted imaging to dynamic contrast-enhanced MRI in the characterization of breast tumors. AJR Am J Roentgenol. 2011;196:210–217.
21. Yabuuchi H, Matsuo Y, Okafuji T, Kamitani T, Soeda H, Setoguchi T, Sakai S, Hatakenaka M, Kubo M, Sadanaga N, Yamamoto H, Honda H. Enhanced mass on contrast-enhanced breast MR imaging: lesion characterization using combination of dynamic contrast-enhanced and diffusion-weighted MR images. J Magn Reson Imaging. 2008;28:1157–1165.
22. El Khouli RH, Jacobs MA, Mezban SD, Huang P, Kamel IR, Macura KJ, Bluemke DA. Diffusion-weighted imaging improves the diagnostic accuracy of conventional 3.0-T breast MR imaging. Radiology. 2010;256:64–73.
23. Le Bihan D, Breton E, Lallemand D, Aubin ML, Vignaud J, Laval-Jeantet M. Separation of diffusion and perfusion in intravoxel incoherent motion MR imaging. Radiology. 1988;168:497–505.
24. Iima M, Le Bihan D. Clinical intravoxel incoherent motion and diffusion MR imaging: past, present, and future. Radiology. 2016;278:13–32.
25. Iima M, Yano K, Kataoka M, Umehana M, Murata K, Kanao S, Togashi K, Le Bihan D. Quantitative non-Gaussian diffusion and intravoxel incoherent motion magnetic resonance imaging differentiation of malignant and benign breast lesions. Invest Radiol. 2015;50:205–211.
26. Bokacheva L, Kaplan JB, Giri DD, Patil S, Gnanasigamani M, Nyman CG, Deasy JO, Morris EA, Thakur SB. Intravoxel incoherent motion diffusion-weighted MRI at 3.0T differentiates malignant breast lesions from benign lesions and breast parenchyma. J Magn Reson Imaging. 2014;40:813–823.
27. Ma D, Lu F, Zou X, Zhang H, Li Y, Zhang L, Chen L, Qin D, Wang B. Intravoxel incoherent motion diffusion-weighted imaging as an adjunct to dynamic contrast-enhanced MRI to improve accuracy of the differential diagnosis of benign and malignant breast lesions. Magn Reson Imaging. 2017;36:175–179.
28. Liu C, Wang K, Chan Q, Liu Z, Zhang J, He H, Zhang S, Liang C. Intravoxel incoherent motion MR imaging for breast lesions: comparison and correlation with pharmacokinetic evaluation from dynamic contrast-enhanced MR imaging. Eur Radiol. 2016;26:3888–3898.
29. Jiang L, Lu X, Hua B, Gao J, Zheng D, Zhou Y. Intravoxel incoherent motion diffusion-weighted imaging versus dynamic contrast-enhanced magnetic resonance imaging: comparison of the diagnostic performance of perfusion-related parameters in breast. J Comput Assist Tomogr. 2018;42:6–11.
30. Liu C, Liang C, Liu Z, Zhang S, Huang B. Intravoxel incoherent motion (IVIM) in evaluation of breast lesions: comparison with conventional DWI. Eur J Radiol. 2013;82:e782–9.
31. Dijkstra H, Dorrius MD, Wielema M, Pijnappel RM, Oudkerk M, Sijens PE. Quantitative DWI implemented after DCE-MRI yields increased specificity for BI-RADS 3 and 4 breast lesions. J Magn Reson Imaging. 2016;44:1642–1649.
32. Iima M, Kataoka M, Kanao S, Onishi N, Kawai M, Ohashi A, Sakaguchi R, Toi M, Togashi K. Intravoxel incoherent motion and quantitative non-Gaussian diffusion MR imaging: evaluation of the diagnostic and prognostic value of several markers of malignant and benign breast lesions. Radiology. 2018;287:432–441.
33. Cho GY, Gennaro L, Sutton EJ, Zabor EC, Zhang Z, Giri D, Moy L, Sodickson DK, Morris EA, Sigmund EE, Thakur SB. Intravoxel incoherent motion (IVIM) histogram biomarkers for prediction of neoadjuvant treatment response in breast cancer patients. Eur J Radiol Open. 2017;4:101–107.
34. Kim Y, Kim SH, Lee HW, Song BJ, Kang BJ, Lee A, Nam Y. Intravoxel incoherent motion diffusion-weighted MRI for predicting response to neoadjuvant chemotherapy in breast cancer. Magn Reson Imaging. 2018;48:27–33.
35. Che S, Zhao X, Ou Y, Li J, Wang M, Wu B, Zhou C. Role of the intravoxel incoherent motion diffusion weighted imaging in the pre-treatment prediction and early response monitoring to neoadjuvant chemotherapy in locally advanced breast cancer. Medicine. 2016;95:e2420.

36. Cho GY, Moy L, Zhang JL, Baete S, Lattanzi R, Moccaldi M, Babb JS, Kim S, Sodickson DK, Sigmund EE. Comparison of fitting methods and b-value sampling strategies for intravoxel incoherent motion in breast cancer. Magn Reson Med. 2015;74:1077–1085.

37. Doudou NR, Liu Y, Kampo S, Zhang K, Dai Y, Wang S. Optimization of intravoxel incoherent motion (IVIM): variability of parameters measurements using a reduced distribution of b values for breast tumors analysis. MAGMA. 2019 [Epub ahead of print].

38. Jalnefjord O, Montelius M, Starck G, Ljungberg M. Optimization of b-value schemes for estimation of the diffusion coefficient and the perfusion fraction with segmented intravoxel incoherent motion model fitting. Magn Reson Med. 2019;82:1541–1552.

39. Kroeker RM, Henkelman RM. Analysis of biological NMR relaxation data with continuous distributions of relaxation times. J Magn Reson. 1986;69:218–235.

40. Tudorica LA, Oh KY, Roy N, Kettler MD, Chen Y, Hemmingson SL, Afzal A, Grinstead JW, Laub G, Li X, Huang W. A feasible high spatiotemporal resolution breast DCE-MRI protocol for clinical settings. Magn Reson Imaging. 2012;30:1257–1267.

41. Hastie T, Tibshirani R, Friedman J. The elements of statistical learning. Data mining, inference, and prediction. 2nd ed. NY, NY: Springer; 2009.

42. Tudorica A, Oh KY, Chui SYC, Roy N, Troxell ML, Naik A, Kemmer K, Chen Y, Holtorf ML, Afzal A, Springer CS, Li X, Huang W. Early prediction and evaluation of breast cancer response to neoadjuvant chemotherapy using quantitative DCE-MRI. Transl Oncol. 2016;9:8–17.

43. Yankeelov TE, Rooney WD, Li X, Springer CS. Variation of the relaxographic "shutter-speed" for transcytolemmal water exchange affects the CR bolus-tracking curve shape. Magn Reson Med. 2003;50:1151–1169.

44. Li X, Rooney WD, Springer CS. A unified magnetic resonance imaging pharmacokinetic theory: intravascular and extracellular contrast reagents. Magn Reson Med. 2005;54:1351–1359.

45. Cortes C, Vapnik V. Support-vector networks. Mach Learn. 1995;20:273–297.

46. Hanley JA, McNeil BA. A method of comparing the areas under receiver operating characteristic curves derived from the same cases. Radiology. 1983;148:839–843.

47. Dietrich O, Raya JG, Reeder SB, Reiser MF, Schoenberg SO. Measurement of signal-to-noise ratios in MR images: influence of multichannel coils, parallel imaging, and reconstruction filters. J Magn Reson Imaging. 2007;26:375–385.

48. Tofts PS, Brix G, Buckley DL, Evelhoch JL, Henderson E, Knopp MV, Larsson HBW, Lee T-Y, Mayr NA, Parker GJM, Port RE, Taylor J, Weisskoff RM. Estimating kinetic parameters from dynamic contrast-enhanced T1-weighted MRI of a diffusable tracer: standardized quantities and symbols. J Magn Reson Imaging. 1999;10:223–232.

49. Huang W, Li X, Chen Y, Li X, Chang M-C, Oborski MJ, Malyarenko DI, Muzi M, Jajamovich GH, Fedorov A, Tudorica A, Gupta SN, Laymon CM, Marro KI, Dyvorne HA, Miller JV, Barbodiak DP, Chenevert TL, Yankeelov TE, Mountz JM, Kinahan PE, Kikinis R, Taouli B, Fennessy F, Kalpathy-Cramer J. Variations of dynamic contrast-enhanced magnetic resonance imaging in evaluation of breast cancer therapy response: a multicenter data analysis challenge. Transl Oncol. 2014;7:153–166.

50. Jensen JH, Helpern JA, Ramani A, Lu H, Kaczynski K. Diffusional kurtosis imaging: the quantification of non-Gaussian water diffusion by means of magnetic resonance imaging. Magn Reson Med. 2005;53:1432–1440.